ELSEVIER

Materials Science and Engineering A342 (2003) 192–200

MATERIALS SCIENCE & ENGINEERING A

www.elsevier.com/locate/msea

Interfacial adhesion of laser clad functionally graded materials

Y.T. Pei, V. Ocelík, J.Th.M. De Hosson *

Department of Applied Physics, Materials Science Center and the Netherlands Institute for Metals Research, University of Groningen, Nijenborgh 4, 9747 AG Groningen, The Netherlands

Received 9 January 2002; received in revised form 23 April 2002

Abstract

Specially designed samples of laser clad $AlSi_{40}$ functionally graded materials (FGM) are made for evaluating the interfacial adhesion. To obtain the interfacial bond strength notches are made right at the interface of the FGMs. In-situ microstructural observations during straining in a field-emission gun environmental scanning electron microscopy reveal different failure modes of the FGMs and substrate. Mapping of strain fields using digital imaging correlation shows a gradual transition of deformation over the interface region and softening effects in the heat-affected zones of the FGM tracks. The strengthening of the FGM is dominated by the size of the Al halos around the particles, in accordance with a dislocation pile-up model.

Keywords: Functionally graded coatings; Interface; Adhesion; Al–Si alloys; Scanning electron microscopy; Digital image correlation

1. Introduction

The term 'functionally graded materials' (FGMs) is now widely used by the materials community for a class of materials exhibiting spatially inhomogeneous microstructures and properties. Graded materials in themselves are not something new, but what is exciting about them is the realization that gradients can be designed at a microstructural level to tailor specific materials for their functional performance in particular applications. Therefore, a possible approach for eliminating the sharp interface present in laser surface cladding (LSC) is to introduce the concept of FGMs into the design of coating structure. In general, the performance of a coating depends in many applications on the bond strength between coating and substrate material. Consequently, it is essential to quantify the adhesive strength of a coating so as to guarantee the functionality of the material system. The actual strength of a coating/substrate interface is governed by a number of variables such as, the elastic mismatch between dissimilar materials, the possible plastic flow, the residual stresses and defects introduced into the coating, the substrate and near the interface. Actually, it is already difficult to find a generally accepted definition of adhesion between coating and substrate that takes into account the complexity of the effects of the microstructure, external loading and the environment. Several methods exist to determine the interfacial bond strength of coatings, such as the direct pull test, bend test, scratch and indentation tests, impact test, cavitation test and Rockwell imprint test. However, none of these tests is accurate enough to provide detailed information about adhesion properties in various types of coatings. Indeed, they even show contradictory results on the same type of coatings, as reported by Ollendorf and Schneider [1]. Nevertheless, among these various tests direct pull and bending tests are frequently used. In the direct pull test as defined in the ASTM D4541 and ASTM C633-79, failure often occurs at the location of the polymeric adhesive that is applied on top of the coating. Further, although four-point flexure test is suitable to evaluate the adhesive strength between the ceramic/metal interfaces (Cr_2O_3/steel) produced by laser processing [2], this method may not work on systems with a very strong interface. With such an interface the pre-crack propagates directly across the interface, and no delamination occurs between the coating and the substrate.

* Corresponding author. Tel.: +31-503634898; fax: +31-503634881
E-mail address: hossonj@phys.rug.nl (J.T.M. De Hosson).

0921-5093/02/$ - see front matter
PII: S0921-5093(02)00249-6

It is well known that laser surface engineering may form a strong bond between a coating and the substrate material [3–5]. In particular, we have recently produced FGMs by laser cladding [6], in which a progressive change in both microstructure and related properties is achieved as a function of depth. The strength of such an interface in FGMs cannot be measured by a direct pull test on the specimen with a clamp attached to it because the interface is stronger than available adhesives. This paper concentrates on a specially designed specimen so as to allow a direct pull test on the as-coated samples without the necessity of any attachment Furthermore, digital image correlation (DIC) technique is used to study the deformation behavior of both the FGM and the substrate near the interface during tensile tests. It is applied to examine whether or not a gradual transition in mechanical properties is realized between the laser-clad FGMs and the substrate.

2. Experimental details

The specimens are fabricated by a one-step laser cladding technique, in which AlSi-based FGMs of 1.5–2.5 mm thickness are coated on an Al-alloy substrate [6]. The laser-clad samples are (see Fig. 1a), such that the FGM track just fills in the grooved substrate as a whole. Tensile specimens are then cut from the clad samples by spark erosion (see Fig. 1a). After finishing a tensile specimen, the FGM track looks like a weld located at the center of the specimen and perpendicular to the tensile loading direction, as illustrated in Fig. 1(b). This configuration ensures that the interfaces between the FGM track and the substrates on both sides are under an applied load during the tensile test. After further machining of the test specimens, a notch can be made right at the interface. The notches have a hyperbolic cross section.

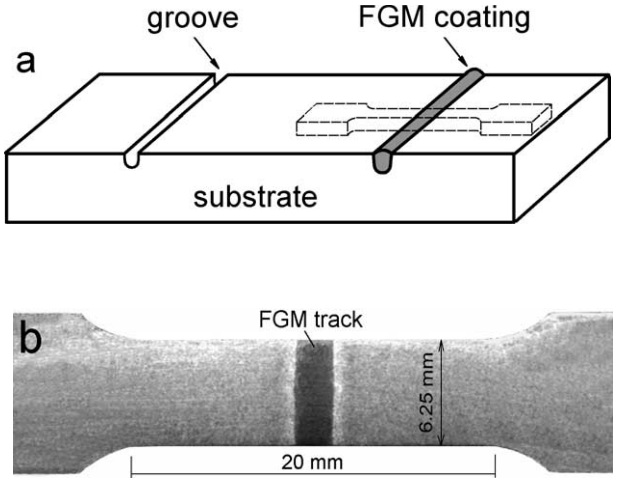

Fig. 1. (a) Sketch of sample preparation and (b) top view of a prepared tensile specimen without notches.

In this work a Rofin CW020-type 2 kW Nd:YAG laser is applied to produce the FGM coating tracks. The focal length of the lens is 100 mm, but the lens is operated at a defocusing distance of +9 mm with a 2.5 mm spot in diameter on the surface of the substrate. A numerically controlled x–y table executes the movement of the specimen. The powder feeder apparatus is a Metco 9MP instrument. The details of the setup for laser cladding are given in reference [6]. The processing parameters are 2000 W laser power, 7 mm s^{-1} scanning speed and 10–30 g min^{-1} powder feeding rate. The shielding gas is helium with a flow rate of 0.167 l s^{-1}.

Aluminum-based substrates are cut from a cast piston of a commercial AlSi-alloy with a nominal composition (wt.%): 11.94 Si, 1.19 Mg, 1.08 Cu, 0.89 Ni, 0.62 Fe, 0.27 Mn and the balance being Al. Two grooves with 2.2 mm open width and 1.5 mm depth are made by electric discharge cutting on the flat substrates $100 \times 50 \times 10$ mm^3 in size. The coating material is Al–40wt.%Si alloy powder with a particle size of 50–125 μm.

According to the ASTM standard A370, the tensile specimen dimensions are modified in order to fit the tensile stage inside the chamber of a scanning electron microscope (SEM). Specimen dimensions are length 20 mm and width 6.25 mm. The thickness of the specimens varied from 0.9 to 1.0 mm. All the FGM specimens are naturally aged for 1 month before tensile tests.

The specimens are loaded using the special stage (Kammrath & Weiss GmbH) mounted inside an environmental scanning electron microscope equipped with a field-emission gun (Philips E-SEM XL30 FEG) or under an optical microscope (OM). A fixed speed of 0.5 μm s^{-1} is used in all the tensile tests. A series of digitized optical micrographs are stored at constant time intervals and are fed into the DIC software (so-called Aramis) of GOM GMBH, where the displacements and the strain fields are computed. For an overview of the strain field over the whole gauge area, very fine dots of black paint are sprayed onto the specimen surface, the image of which is captured by a CCD camera for optimized contrast images during deformation.

The principle of DIC is based on the correlation between micro-features in a *source* image taken prior to deformation and the corresponding displaced markers in a so-called *destination* image [7,8]. For the sake of comparison, a commercial video extensometer of MESSPHYSIK ME46 is used to examine the axial stain distribution over the whole gauge length of the specimens. The extensometer could simultaneously monitor the elongation of nine segments, which makes it possible to study the overall deformation behavior of both the clad FGMs and the substrate materials under tensile stress.

3. Results

The typical microstructure over the interface region of the proposed samples is shown in Fig. 2(a). The transition from the substrate to the $AlSi_{40}$ FGM is smooth and gradual: fine α-Al dendrites nucleate and grow on the original coarse Al dendrites in the substrate; primary Si particles appear at a distance of about 50 μm from the molten boundary, which covers a particle-free zone. In the FGM the discrete Si crystals surrounded by α-Al dendritic halos increase continuously in size and volume fraction as a function of the distance from the boundary, from 5 μm and 21 vol.% near the boundary to 48 μm and 35 vol.% at the center of the FGM track, respectively. In contrast, the α-Al halos exhibit less change in size over the same distance. The width of the particle-free zone, ranging from 20 to 50 μm, is mainly controlled by the temperature gradient and the scan velocity of the laser beam.

Due to the difference between the melting temperature of the α-Al phase and the AlSi eutectic temperature, the molten boundary is rough at a micro-scale and the roughness is governed by the geometry and size of the coarse Al dendrites in the substrate. The secondary arm spacing of the coarse Al dendrites is found to be 40 μm and the melt depth between the secondary arms may reach 25 μm, depending on the inclined angle of the arms with respect to the molten boundary. Fig. 2(b) exhibits the microstructure of the normal FGM clad on the top surface of a substrate. A very similar transition over the molten boundary and the graded microstructure can be seen as observed in Fig. 2(a).

Tensile tests of all ten specimens without a notch exhibit fracture in the substrate material, i.e. outside the laser clad $AlSi_{40}$ FGM tracks. It means that both the strength of the FGM tracks and their interfacial adhesion are higher than the ultimate tensile strength (UTS) of the substrate. Seven specimens fractured approximately 1.5 mm away from the FGM track, as shown in Fig. 3(a). The rest exhibits fracture at random positions far away from the track. During tensile tests the strain–stress curves keep the linear character until a uni-axial deformation of 0.14% at the tensile stress of approximately 125 MPa. Then plastic deformation appears and the final fracture occurs suddenly at a strain of 0.4–0.5%.

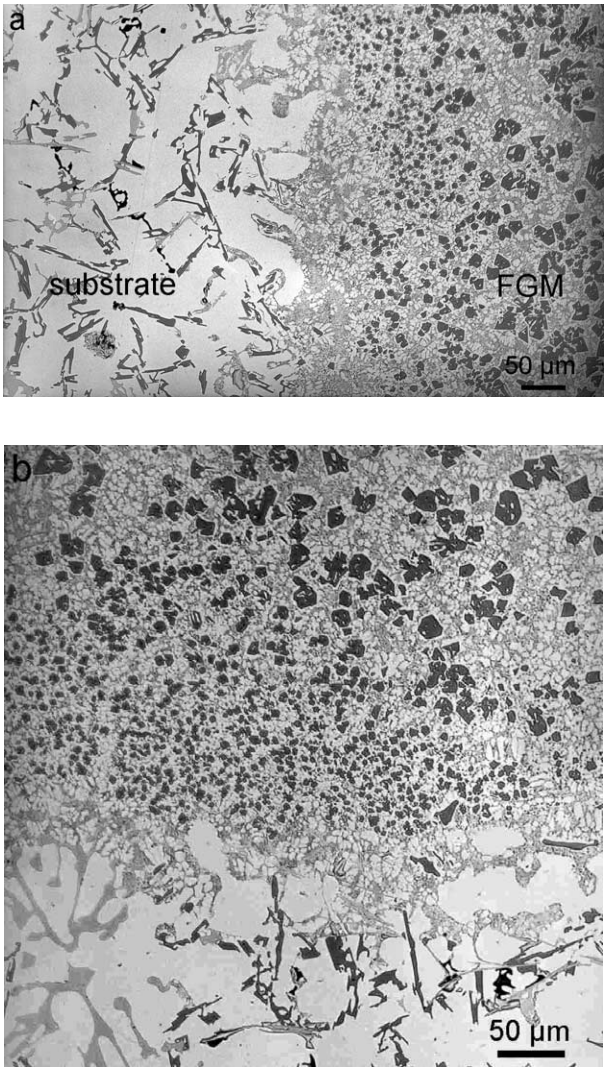

Fig. 2. (a) Microstructure of $AlSi_{40}$ FGM and (b) the longitudinal cross-section of an $AlSi_{40}$ FGM track clad on the surface of the substrate (3000 W laser power, 25 mm s^{-1} beam speed).

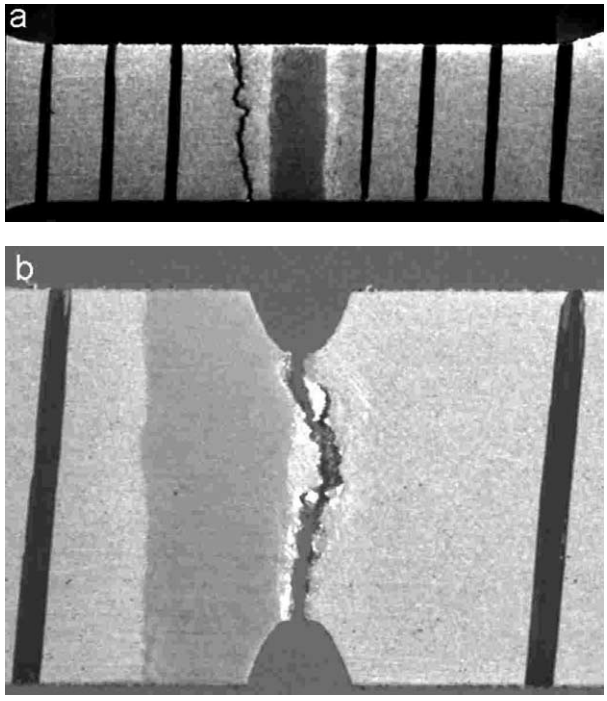

Fig. 3. (a) Fracture near the boundary of HAZ in an unnotched sample and (b) fracture at the interface near the notches. The black straight lines are markers for the video extensometer set-up.

Although the experiments with unnotched specimens have demonstrated the rather strong adhesion of the FGM tracks to the substrate, it still remains uncertain how far the adhesive strength lies above the UTS value of the substrate. No failure could be observed directly at the interfaces during these tensile tests. Therefore, V-notches are made right at the interface. Eight tensile tests are performed with the notched and unnotched specimens, respectively, of the same substrate material in order to determine experimentally the stress concentration factor, which is found to be 1.26. The interfacial strength of the FGM tracks of the notched samples is given in Table 1. The global failure initiates at the notch tip and follows the interface, as seen in Fig. 3(b). However, the main crack is often deflected into the heat-affected zone (HAZ) of the substrate, which is obviously related to the difference in strength. To provide insight into the different levels of UTS, tensile tests are also performed on the specimens of both the original cast substrate materials and the pure $AlSi_{40}$ FGM layer produced by 25 overlapping laser tracks on the substrate. The specimens of the pure $AlSi_{40}$ FGM layer are cut out by spark erosion from the substrate in such a way that all the laser tracks are perpendicular to the loading direction, and no notches are employed. The results are also listed in Table 1. It is clear that the interfacial strength of the FGM tracks is 22% above the UTS of the substrates and is very close to the UTS of the FGMs.

In order to study the deformation behavior of the FGM tracks with respect to the substrate, DIC measurements are applied. A typical axial strain field over the gauge without a notch is presented in Fig. 4. The FGM track shows homogenous strain fields and a gradual strain transition over the interface. In contrast, the substrate exhibits rather inhomogeneous strain fields that consist of locally deformed areas, which may develop as potential sites of failure. In particular, softening effects are clearly observed in the heat-affected zones (HAZs) of the substrate even at the early stages of deformation. The outer regions of the HAZs, which are adjacent to the thermally undisturbed substrates, exhibit the highest strain levels during tensile tests and may initiate the final fracture in most cases. About 70% of the tensile samples fracture at the outer region of the HAZs, where the UTS value of the substrate material is reached.

Table 1
Bond strength of FGM and substrate

	Strength (MPa)	S.D. (MPa)
$AlSi_{40}$ FGMs	272.8	16.2
Interface	258.5	17.4
Substrate	212.6	13.8

A detailed field of elastic strain over the interface region of an FGM track is shown in Fig. 6(a). The strain field is measured at a tensile stress of 116.7MPa, which is still lower than the macro yield stress of the sample. Dense iso-strain lines are seen in the interfacial region which run parallel to the interface. For overall patterns of the lines see also Fig. 4(c)Fig. 5(a). These parallel iso-strain lines show an almost constant interval in the vicinity of the bond region of the FGM track and become less dense towards the interior of the track. By extracting the strain values at a certain section, one may estimate the variation of the stiffness of the FGMs across the interface (see Fig. 6b). Fig. 7 presents the axial strain distribution over the whole gauge length, which is measured with the video-extensometer. On the inset, the black markers divide the gauge length into nine segments. Segment No.5 covers the FGM track and, segments No. 4 and 6 correspond to the HAZs on both sides of the track. Because the extensometer measures the elongations by scanning 50–70 horizontal lines, the measured values are just the average strain of a segment. From Fig. 7, it can be seen that the HAZs are heavily deformed and that the FGM track shows an extremely low strain value. The final fracture initiates in segment No.4, where the highest strain value is measured. This result corresponds to the DIC measurements of the strain field.

SEM in-situ observations during tensile tests revealed the same mechanism of crack initiation and propagation at both cases where the fracture occurred at the HAZ outer boundary and far away from the HAZ, respectively. Cracks mainly resulted from decohesion of the large Si or $AlCu_2$ plates from the Al matrix, as seen in Fig. 8(a). These plate-like precipitates have a maximum size of about 100 μm in length and a few μm in width. In order to distinguish the different failure mode of the laser clad $AlSi_{40}$ FGMs, SEM in-situ observations during tensile tests are performed on the unnotched samples of the pure $AlSi_{40}$ FGM produced by the laser cladding technique. These observations revealed that failure initiation in the FGMs is dominated by cracking of Si particles. Fig. 9 shows typical cracked Si particles after the onset of the plastic deformation of the coating. The opening of the crack surfaces leads to voids nucleation in the adjacent Al-halos, see Fig. 9(b). Most of the cracked particles tend to align their fracture plane perpendicular to the loading direction. On the other hand, the cracked Si particles are randomly distributed and can be found anywhere from the edge to the center of the gauge. It is often observed that the surrounding particles of a cracked particle might not crack until a much higher deformation level is reached, during which new cracked particles appear somewhere else. It is almost impossible to predict the position where fracture occurs in the unnotched samples. Although it is impossible to observe directly the actual size of the

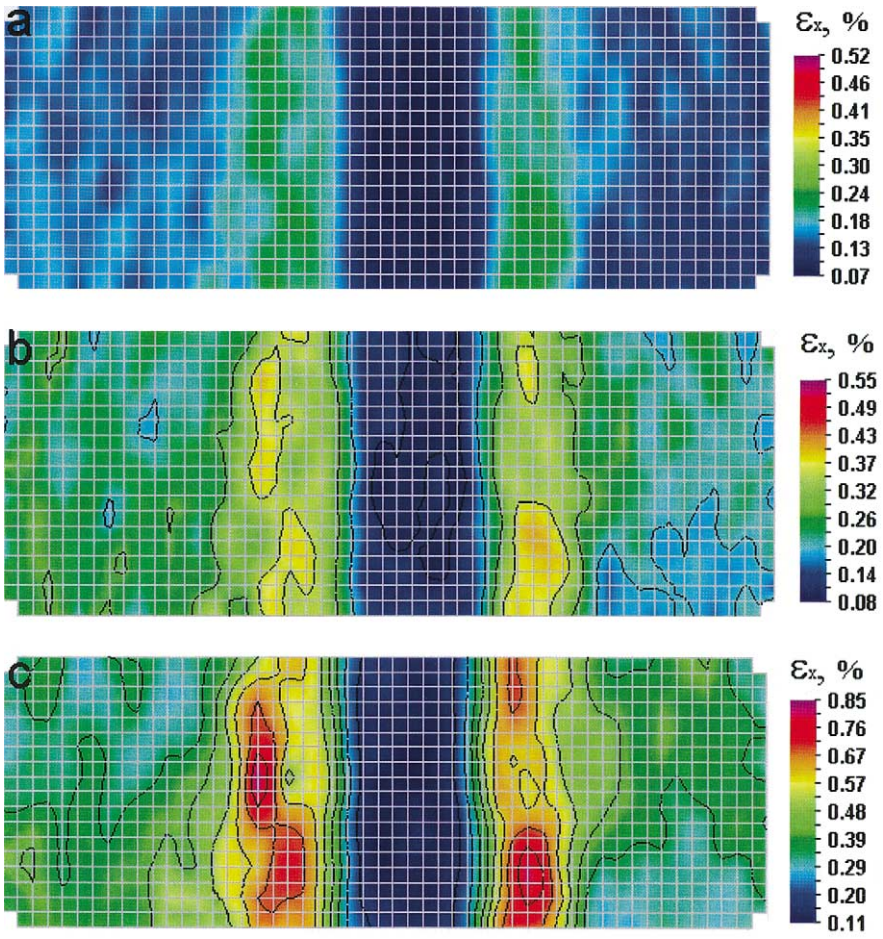

Fig. 4. Evolution of the axial strain field measured by DIC on a laser clad FGM specimen at different applied tensile stresses: (a) 117.5 MPa; (b) 166.3 Mpa; and (c) 190.4 MPa. The cell size of the grid is 0.28 mm.

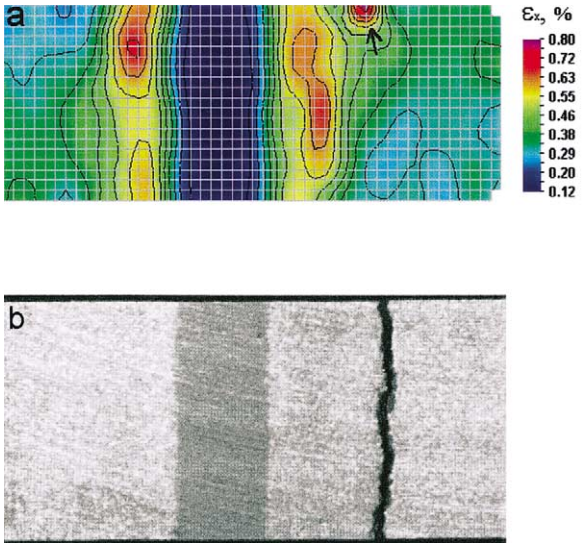

Fig. 5. Strain field (a) showing crack initiation, indicated by an arrow, far away from the FGM track. The destination image for obtaining this figure was recorded just prior to the fracture; (b) fractured sample.

particles on 2D projections, the particle size seems not to be a strong factor for cracking because both small and large broken particles often co-exist. Nevertheless, it is considered that the final fracture results from the growth and linkage of voids that initiate at the cracked particles.

The fractography present in Fig. 10 shows both flat fracture planes of the particles and dense micro-dimples in the Al-halos around the Si particles. The tip corners of the Si_p stay undamaged. In contrast, the fracture surface of the substrate exhibits large smooth areas due to decohesion of the hard plate-like phases from the matrix, see Fig. 8(b).

4. Discussion

One may argue that the adhesion of an FGM coating to the substrate may not be the same as the adhesion in our specially designed samples, when the FGM fills a groove as shown in Fig. 1(a). However, the consistency of the microstructure over the transition areas between

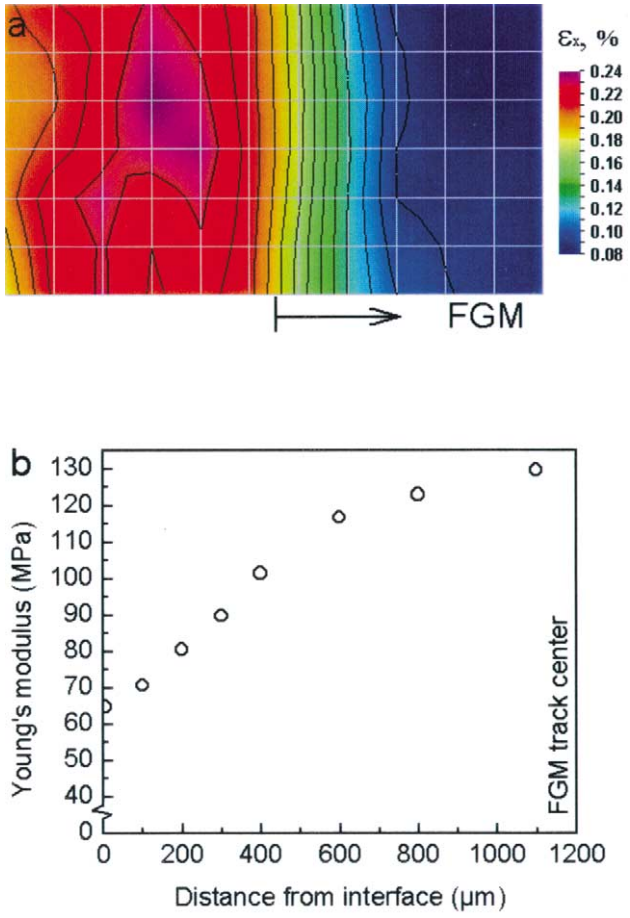

Fig. 6. (a) Detailed strain field over the interface region of an FGM track under an applied tensile stress of 116.7 MPa and (b) the corresponding profile of the stiffness.

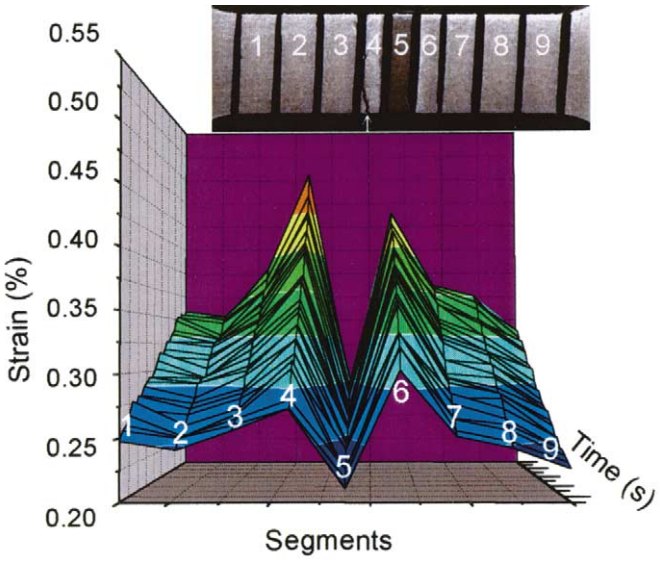

Fig. 7. Strain-time curves of the various segments over the gauge length measured by the video-extensometer. The optical micrograph indicates the segments on the specimen and an arrow indicates the main crack in segment No.4.

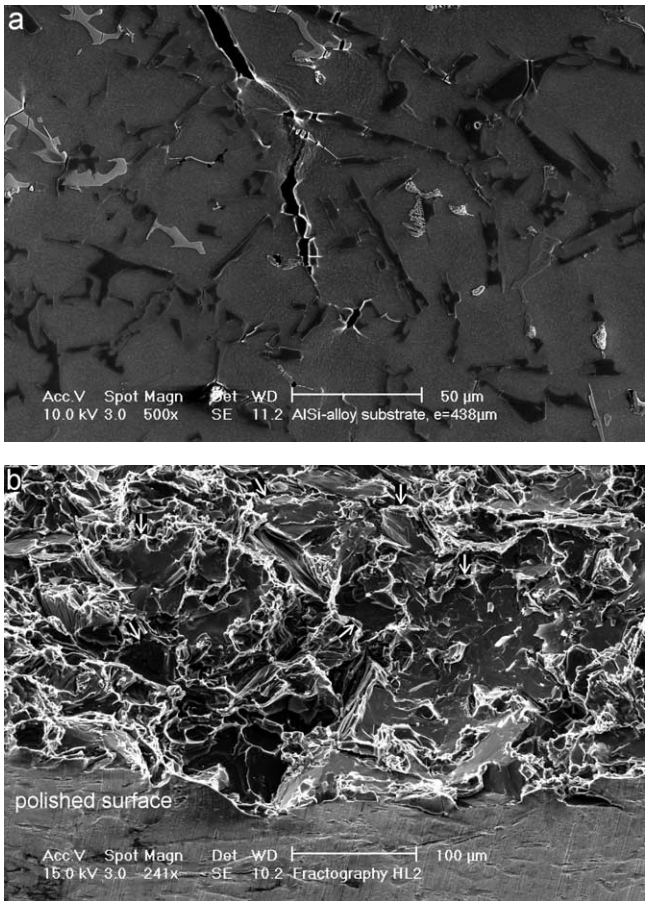

Fig. 8. (a) In-situ SEM observation showing crack initiation and propagation along the plates in the substrate under a tensile load in the horizontal direction; (b) fractography showing smooth areas on the fracture surface due to decohesion of plates.

the FGM and the substrate in both cases mentioned above is clearly documented in Fig. 2(a) and (b). Microstructural similarity between the proposed samples and the FGM coating tracks [6] supports the validity of the method for the FGMs in this particular case.

Rough interfaces are formed in laser clad $AlSi_{40}$ FGMs by inhomogeneously remelting a surface layer of the substrate materials due to the different melting temperatures of the α-Al dendrites and AlSi eutectics. Such interfacial roughness promotes a good mechanical locking of the coating to the substrate. Unlike the situations in sprayed thermal barrier coatings (TBCs) [9,10], the alternating stresses at the peaks and valleys along the interface are restricted after cooling due to two main reasons. The particle-free zone has the same chemical composition and thermal expansion coefficient. The elastic modulus is equal to the elastic modulus of the bulk substrate. This is because the thin layer of the substrate does not mix with the melt of the coating material. Secondly, the gradual changes in volume fraction of Si particles suggest a graded thermal expansion coefficient and elastic modulus. It gives good

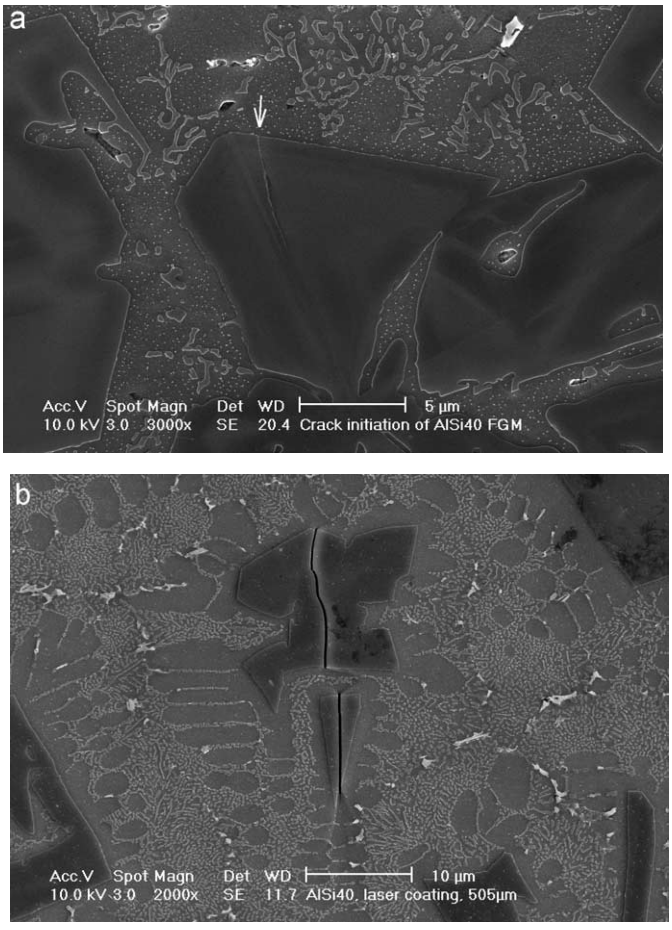

Fig. 9. (a) In situ observations of crack initiation in a Si particle, indicated by an arrow, and (b) cracked Si particles in the $AlSi_{40}$ FGMs.

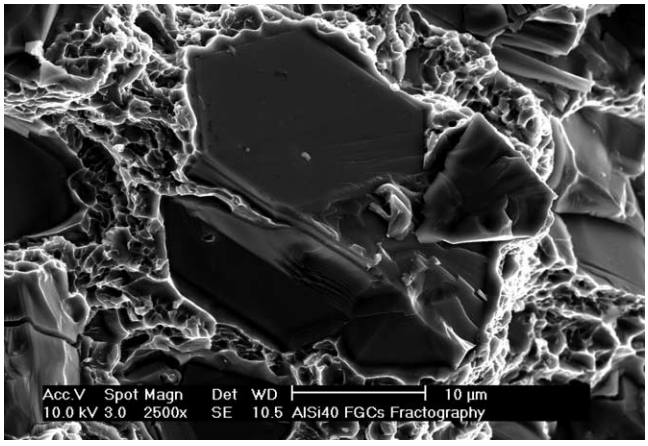

Fig. 10. Fractography of $AlSi_{40}$ FGM showing the cleaved Si particles and micro-dimples in the surrounding Al-halos.

conditions for a low gradient of the residual stress in the coating and in the region between coating and bulk substrate. On the other hand, the roughness increases the total area of the interface by a factor of 1.68, assuming a half-period sinusoidal profile with amplitude of 25 μm and half-wavelength of 40 μm. Such an increase is expected to contribute to the interfacial bond strength compared to a straight interface.

In particle reinforced metal matrix composites fracture initiation is mainly associated with particle fracture and particle-matrix interfacial failure, depending on the particular composite and matrix conditions [11–15]. There are numerous models proposed to describe the crack initiation of the particles, mainly based on three different criteria, i.e. stress criterion, strain criterion and energy criterion [11–14]. These models also have different mechanism, that is to say, some of them are derived from continuum mechanics and some are based on dislocation theory. With respect to the general behavior of particle cracking, several features may be summarized here: (1) the number of cracked particles increases as the stress or strain increases; (2) lenticular particles crack more easily than spherical particles; and (3) the stress required for particle cracking decreases as particle size increases. In addition, Lloyd [15] observed that fracture initiates more easily in clusters of particles that are ineluctable in the fabrication with the molten metal route. Initiated by particle cracking and/or decohesion of the matrix between the particles within the clusters, final fracture is achieved by fracture through the matrix. Because of localization of damage and very limited void growth, the reason of failure is the intensification of a large triaxial stress state exerted on the matrix. Such clustering factor does not play an important role in our case, because the Si particles in the FGMs are well separated by the Al-halos and the adjacent eutectics. This is controlled by the nucleation events and growth process of Si_p in the laser pool [16,17]. What is important for Si_p cracking appears to be the size of the Al-halos.

In plastically heterogeneous materials such as the $AlSi_{40}$ FGMs, the activity of dislocation sources generates dislocation pile-ups in the ductile phase. The pile-up of dislocations will continue until a critical stress is reached at the spearhead of the pile-up. The stress may generate either plastic flow or fracture in the particles. The equivalent normal stress, σ_{eff}, acting on the particle by the pile-up is proportional to the length of the pile-up and the applied tensile stress squared [13]. In $AlSi_{40}$ FGMs, the length of the pile-up is limited to the sizes of Al-halos because the eutectics are considered to be nontransparent for slip. As shown in [6] the α-Al halos surrounding the Si_p in the lower part of a FGM coating are thinner than those in the upper part. Another notable feature is that the dendritic nature of the α-Al halos is more fully developed further from the bottom of the track. This is considered to be additional evidence that their growth rate increases with decreasing depth in the melt pool. These observed characteristics suggest that the size of the halos is limited by both their growth

rate and by the time necessary to reach the temperature at which the eutectic finally forms.

The average size of the Al-halos in $AlSi_{40}$ FGMs is between 3 and 10 μm, i.e. one or two orders of magnitude smaller than the size of Al dendrites in the substrate materials. It suggests that a much higher tensile stress is necessary to generate cracks in the particle. However, to know the real stress in the particles under an applied load, it is necessary to also consider the misfit stress that is due to the difference in the thermal expansion coefficient between Si particles and Al matrix [18]. The particles are actually under a hydrostatical compressive stress of the order of the yield stress of the matrix, even when no external stress is applied to the materials. At an applied tensile stress just above the yield stress of the matrix, the net normal stress acting on the particles in the loading direction is approximately zero. This leaves the particles under the sole effect of the stresses arising from the plastic deformation, which may explain the fact that Si particles start to crack immediately after the onset of plastic deformation.

Softening of HAZs is often reported as an accompanying effect of welds in age hardened or strain hardened Al-alloys due to the microstructural change of the areas exposed to the heat input. Commonly, the softening effect is examined with hardness measurements where the hardness profile exhibits a drop in HAZs [19]. For Al-alloys with a high concentration of alloying elements, however, it may be questionable to detect softening effects with hardness measurements because of inhomogeneities. The softening phenomenon in the HAZs of laser clad FGMs can be observed by strain mapping with the DIC technique, which reveals directly the different deformation resistance of the FGMs, HAZs and the undistorted substrate materials subjected to the applied tensile stress.

In the study of welds, the properties of the HAZs are usually expressed either as a function of exposed peak temperature or as a function of distance from the fusion boundary. It has been shown that the maximum loss in hardness of the HAZs corresponds to a relatively low peak temperature at which over-aging occurs, rather than the higher peak temperatures that result in the dissolution of precipitates in the HAZs of 6xxx and 7xxx Al-alloys [19]. In other words, the minimum hardness level in the HAZs always appears at a distance away from the fusion boundary. Natural aging may only recover a part of the reduced hardness/strength of the HAZs. It is the same situation in our case that the maximum strain levels most likely appear at the outer region of the HAZs during deformation, as seen in Fig. 4. The reason for softening here is considered to be the same as in the welds of 6xxx alloys. The Al dendrites in the substrate possess a similar composition to that of the 6xxx alloys and are consequently subjected to similar microstructure changes during the thermal cycle of laser cladding. Another fact that is noteworthy is that the softening of the HAZs is not homogeneous because of the inhomogeneous distribution of particles in the substrate.

5. Conclusions

The specially designed samples of laser clad $AlSi_{40}$ functionally graded materials (FGMs) in a grooved substrate have been examined as a potential configuration for the evaluation of interfacial adhesion of FGMs. Both the UTS and the interfacial bond strength of the $AlSi_{40}$ FGMs are studied, and both appear to be higher than the UTS of the substrate material. With the application of digital imaging correlation techniques, the deformation behavior of both the FGM and the substrate near the interface is clearly revealed. Strain field mapping demonstrates the gradual transition in strain of the FGMs over the interface region and the softening effects in the heat-affected zones of the FGM tracks. In-situ microstructure observations during tensile tests reveal the different failure modes of the FGMs and the substrates, respectively. The strengthening of the FGM is dominated by the size of the Al-halos around the particles, in accordance with a dislocation pile-up model.

Acknowledgements

The Netherlands Institute for Metals Research is acknowledged for its financial support. Dr W.P. Vellinga is acknowledged for the valuable discussion and support on the DIC measurements.

References

[1] H. Ollendorf, D. Schneider, Surf. Coat. Technol. 113 (1999) 86–102.
[2] M.van den Burg, J.T.h.M. De Hosson, Interface Sci. 3 (1995) 107–118.
[3] Y.T. Pei, J.H. Ouyang, T.C. Lei, Metall. Mater. Trans. A 27A (1996) 391–400.
[4] A. Agarwal, N.B. Dahotre, Inter. J. Ref. Mater. Hard Metals 17 (4) (1999) 283–293.
[5] J. Mazumder, in: K.H. Stern (Ed.), Metallurgical and Ceramic Protective Coatings, Chapman and Hall, London, 1996, pp. 74–110.
[6] Y.T. Pei, J.T.h.M. de Hosson, Acta Mater. 48 (2000) 2617–2624.
[7] M.A. Sutton, W.J. Wolters, W.H. Peters, W.F. Ranson, S.R. McNeil, Image Vision Comput. 1 (1983) 133–139.
[8] G. Vendroux, W.G. Knauss, Exp. Mech. 38 (1998) 86–92.
[9] R. Vaßen, G. Kerkhoff, D. Stöver, Mater. Sci. Eng. A303 (2001) 100–109.
[10] M.J. Pindera, J. Aboudi, S.M. Arnold, Mater. Sci. Eng. A284 (2000) 158–175.

[11] Y. Brechet, J.D. Embury, S. Tao, L. Luo, Acta Mater. 39 (1991) 1781–1786.
[12] C.H. Caceres, J.R. Griffiths, Acta Mater. 44 (1996) 25–33.
[13] J.W. Yeh, W.P. Liu, Metall. Mater. Trans. A 27A (1996) 3558–3568.
[14] M. Kouzell, L. Weber, C. san Marchi, A. Mortensen, Acta Mater. 49 (2001) 497–505.
[15] D.J. Lloyd, Acta Mater. 39 (1991) 59–71.
[16] Y.T. Pei, J.T.h.M. de Hosson, Acta Mater. 49 (2001) 561–571.
[17] Templin, Metals Alloys 3 (1932) 136.
[18] R.W. Coade, J.R. Griffiths, B.A. Parker, P.J. Stevens, Phil. Mag. A 44 (1981) 357–372.
[19] A. Hirose, H. Todaka, K.F. Kobayashi, Metall. Mater. Trans. 28A (1997) 2657–2662.